Small pixel hybrid CMOS X-ray detectors

Samuel V. Hull[a], Abraham D. Falcone[a], David N. Burrows[a], Mitchell Wages[a], and Maria McQuaide[a]

[a]Pennsylvania State University, Department of Astronomy and Astrophysics, 525 Davey Lab, University Park, Pennsylvania 16802, United States

ABSTRACT

Next generation X-ray mission concepts (e.g. *Lynx*) call for a wide field X-ray imager with high detection efficiency from 0.2 keV to 10 keV and fast readout capability ($>$ 10 Hz frame rate). In order to properly sample the planned fine angular resolution of the optical assembly (0.5″ HPD), small pixel sizes of less than or equal to 16 microns are required. Hybrid CMOS detectors are a type of active pixel sensor that is well suited to the high throughput and wide bandpass requirements of such instruments, and the pixel size goals are well within reach. In collaboration with Teledyne Imaging Sensors, the Penn State X-ray detector lab has developed new small pixel Hybrid CMOS sensors to meet these needs. These prototype 128 x 128 pixel devices have 12.5 micron pixel pitch, 100 micron fully depleted depth, and include crosstalk-eliminating CTIA amplifiers and in-pixel correlated double sampling capability. We report on characteristics of one of these new detectors, including read noise, energy resolution, and pixel-to-pixel gain variation. The read noise was measured to be as low as 5.54 e^- $\pm$ 0.05 e^-, while the gain variation was found to be 1.12% $\pm$ 0.06%. The energy resolution, including calibration for gain variation, was measured to be as good as 148 eV (2.5%) at 5.9 keV.

Keywords: X-rays, detectors, Hybrid CMOS, Lynx, small pixel, CMOS sensors

1. INTRODUCTION

The *Lynx* X-ray surveyor mission concept[1] for the NASA 2020 Decadal Survey is a promising step for advancing X-ray astrophysics beyond *Chandra*. The concept, which calls for fine (0.5″ HPD) angular resolution mirrors with large effective area ($>$ 2 m^2 at 1 keV), will allow for an extension of X-ray astronomy into the high redshift and low luminosity universe. Further, increased counting statistics for more nearby sources will enable greatly improved spectroscopic and morphological studies. Highlights of specific science goals include studying the birth and growth of the first generation of supermassive black holes, looking for faint absorption lines in the warm-hot intergalactic medium (WHIM), and studying the impact of feedback on stellar birth and evolution.

Because of the very large increase in effective area, even moderately bright sources observed with *Lynx* will cause traditional X-ray charge coupled devices (CCDs) to experience pile-up — whereby two or more photons land in a single pixel before the frame is read out. Faster readout speeds are required to avoid pile-up, which can be realized through active pixel sensor technology such as hybrid CMOS detectors (HCDs).[2] These detectors include in-pixel amplifiers with row-column addressing and the ability to read out individual pixels. Combined with utilization of multiple readout lines, this gives HCDs the ability to read out many times faster than traditional CCDs. Further, the absence of parallel clock gates and elimination of charge transfer across many centimeters of silicon grants HCDs lower power requirements[3] and increased radiation hardness.[4]

Recent development efforts have included the design and fabrication of new small pixel X-ray HCDs that are designed to meet the needs of *Lynx* with small enough pixels to sample the telescope's very fine angular resolution. The 12.5 micron pixel pitch detectors include in-pixel correlated double sampling (CDS) capability and crosstalk-eliminating CTIA amplifiers. In this proceeding we report the status of the small pixel HCD detector characterization and present results on the charge spreading, energy resolution, read noise, and pixel-to-pixel gain variation of one of these devices.

Further author information:
S.V.H.: E-mail: s.hull@psu.edu

High Energy, Optical, and Infrared Detectors for Astronomy VIII, edited by Andrew D. Holland, James Beletic, Proc. of SPIE Vol. 10709, 107090E · © 2018 SPIE
CCC code: 0277-786X/18/$18 · doi: 10.1117/12.2312121

2. THE SMALL PIXEL HYBRID CMOS DETECTORS

X-ray HCDs, which are developed as a joint collaboration between Penn State University (PSU) and Teledyne Imaging Sensors (TIS), are composed of two separate layers: the absorbing silicon layer and the readout integrated circuit (ROIC). The absorbing layer is responsible for photon-to-charge conversion via photoelectric absorption in the silicon pixel array, while the ROIC acts as a charge-to-voltage signal converter and contains all readout circuitry. The layers are precisely aligned and then joined together at each pixel with indium bump bonds. This unique architecture allows for each layer to be independently optimized; the absorbing layer is optimized for high quantum efficiency across the soft X-ray bandpass (0.2-10 keV),[5] while the ROIC is optimized for fast readout and on-chip signal processing.[6] X-ray HCDs also commonly include a thin layer of aluminum deposited directly on top of the silicon absorption layer in order to block optical light.[7] Figure 1 shows a schematic of an X-ray HCD.

The small pixel HCDs are a new prototype X-ray HCD designed specifically to meet the needs of future high throughput X-ray missions with fine angular resolution. Concept studies for *Lynx* call for a High-Definition X-ray Imager (HDXI) instrument that utilizes a large, high speed, silicon pixel array to serve as a wide field X-ray imager with moderate spectral resolution. In order to oversample the PSF of the $0.5''$ HPD mirrors, HDXI requires pixels sizes $\leq 0.33'' \approx 16$ μm. Further, concept studies call for HDXI to obtain near Fano-limited energy resolution (≤ 150 eV at 5.9 keV) and ≤ 4 e^- read noise. Previous generation X-ray HCDs were limited to ≥ 18 μm pixels and read noise $\gtrsim 7$ e^-.[8] The small pixel HCD design therefore aimed to scale down X-ray HCD technology to smaller pixel sizes while improving read noise and energy resolution performance.

These newly developed detectors are 128 x 128 prototype devices with 12.5 micron pitch pixels, and a depletion depth of 100 microns. An easily scalable design allows for future arrays to be fabricated with up to 4k x 4k pixels with multi-side abuttable packages. Below, the key features of the small pixel HCD design are summarized:

CTIA Amplifier: The small pixel ROIC includes a capacitive transimpedance amplifier (CTIA) in each pixel, in contrast to the source follower amplifier of older generation HxRG detectors (e.g. H1RGs, H2RGs, H4RGs). For those older devices, charge collected on the input gate of the source follower is capacitively coupled to neighboring pixels, resulting in a coupled signal present in these pixels which degrades energy resolution. The CTIA instead holds the input gate voltage constant during integration and reduces or removes this effect to immeasurable levels, as has been shown in the Speedster-EXD device.[9]

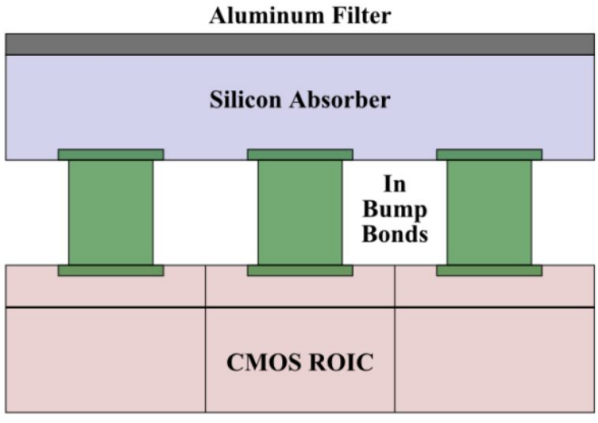

Figure 1. Cross-sectional schematic of an X-ray HCD. Si absorbing layer is bump bonded to the read out electronics layer in each pixel.

Figure 2. Pixel layout of the small pixel HCD test devices. Type A pixel have no in-pixel CDS while type B pixels do include in-pixel CDS.

In-Pixel CDS Subtraction: The small pixel ROIC also includes the option for in-pixel correlated double sampling (CDS) circuitry. The action of resetting a pixel returns the sense node to a variable baseline voltage level, and the uncertainty in this baseline level can lead to an unwanted reset kTC noise. In-pixel CDS enables the subtraction of this variable voltage on-chip prior to integration and before further amplification.

Banded Pixel Layout: The small pixel HCD test device was designed and fabricated in four "banded arrays" of 128 x 32 pixels, which contain four distinct pixel designs for evaluation of pixel performance. The top two bands of each device, or the first 64 rows, contain "Type A" pixels that do not include the in-pixel CDS circuitry. The bottom two bands, or the lower 64 rows, contain "Type B" pixels with the in-pixel CDS. The upper band of each pixel type contains pixels that includes additional shielding in the ROIC for guarding against electrical crosstalk. The lower 32 rows of each pixel type contain standard pixels without this extra shielding. The array layout is shown graphically in Figure 2.

3. EXPERIMENTAL SETUP

We report on testing of one of the small pixel detectors, denoted by its serial number: FPA 18568. FPA 18568 has a 500 Angstrom aluminum filter deposited directly on its absorption layer, and has all the features described in Section 2.

The detector was tested in a modified IR Labs HDL-5 test chamber. The HDL-5 includes a light-tight sealed vacuum section and an unsealed LN2 dewar which is thermally linked to an indium coldfinger in the vacuum section. The detector is mounted in a socket on a small breadboard in the vacuum section as shown in Figure 3. The breadboard mostly serves to route all external signals, while also providing filtering for analog signals. In addition, seven static digital signals (including a signal that determines the pixel type to read out) are set manually by means of jumpers on the board. Two dewar connectors route all lines to an external detector interface board (DIB; developed by TIS) that generates the required power lines and dynamic signals. The detector is configured and read out using the DIB, a Matrox frame frabber, and custom software. The HDL-5 in the full test setup is shown in Figure 4.

The vacuum section of the HDL-5 is evacuated to pressures of 10^{-6} torr, facilitating safe cooling of the detector to cryogenic temperatures via filling the LN2 dewar. The detector temperature is controlled using a silicon diode and heater in concert with a Lake Shore temperature controller, and was maintained at 150 K. A radioactive ^{55}Fe source, producing Mn Kα and Mn Kβ X-ray lines at 5.9 keV and 6.49 keV, was mounted several centimeters from the detector. At a typical operating voltage of 15V applied to the substrate, the detector is fully depleted. Tests were also performed at voltages ranging from 15V to 100V in order to achieve stronger fields and therefore more compact charge clouds within the small pixels.

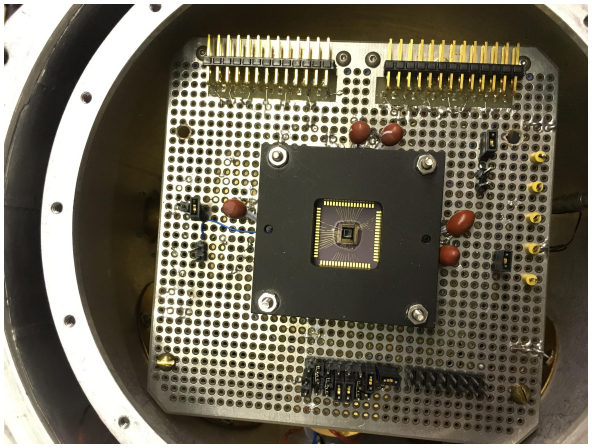

Figure 3. Small pixel FPA test device seated in breadboard inside HDL-5 vacuum section.

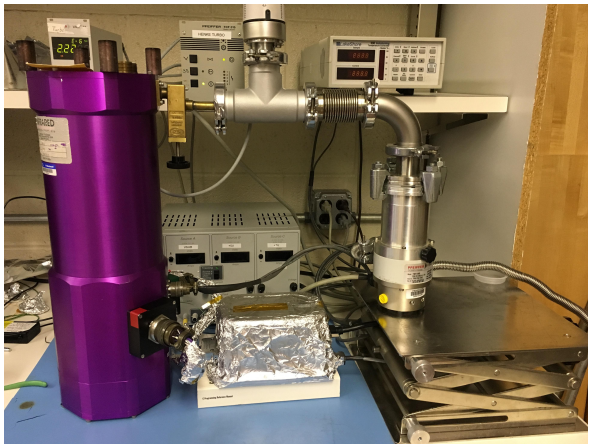

Figure 4. Full HDL-5 test setup featuring the HDL-5 (purple dewar), DIB, and vacuum pumps.

4. DATA REDUCTION

The HDL-5 test stand was used to obtain charge spread, energy resolution, read noise, and pixel-to-pixel gain variation measurements. Data for type A and type B pixels must be acquired separately due to the different output method for each pixel type. Lacking in-pixel CDS, type A pixels must output both a reset and a signal frame for each exposure, which are time multiplexed within one row time. The output is then captured as two 128 x 128 images that have alternating rows of pixel data and zeros; reset frames have pixel data in every even row (numbered starting from zero), while signal frames have pixel data in every odd row. Each frame was then contracted down to 128 x 64 by eliminating zeroed rows, followed by subtraction of the signal frame from the reset frame (these detectors integrate signal voltage down from a high reset level) to create pseudo-CDS images.

Type B pixels already perform on-chip CDS and therefore solely output a 128 x 64 signal frame for each exposure. Before each data run, a bias frame is constructed from the average of 1000 dark frames without an X-ray source. Each output signal frame is subtracted from the bias frame to create bias-subtracted type B frames.

The image subtraction described above removes fixed-pattern noise; however, images may still include horizontal artifacts or "row noise". To remove this non-random noise component a boxcar smoothing algorithm is used that subtracts from each pixel a 21 pixel wide, outlier resistant, moving median value. This results in images that contain only a random pixel noise background.

After boxcar smoothing, we perform X-ray event detection and grading. Event candidates are required to have their primary pixel value above a 5σ threshold, where σ is the read noise (see Section 5.3), and be local maxima in their 3 x 3 pixel region. A secondary threshold, typically between 1σ and 3σ, is then used to select any pixel in the 3 x 3 region above this threshold to be included in the event and have its signal added to the total event signal. Each event is graded according to the number of pixels included and its shape, and then classified using the *Swift* XRT photon counting mode grading scheme.[10] Due to the small pixel size and large depletion depth of these detectors, natural charge spreading was found to be quite high, especially at lower substrate voltages (see Section 5.1) and the grade list was expanded to include additional event geometries. In this proceeding, we use grade 0 events (all charge contained in a single pixel), grade 1 to 4 events (charge spreads to one adjacent pixel), as well as all real X-ray event grades (charge spreads to as many as 7 adjacent pixels).

We also choose to exclude any events that fall on a bad or flickering pixel (or in their 3 x 3 region). These are pixels that are either insensitive to X-rays (inactive pixels), have large deviations from the mean background level, or spend a significant amount of time at large deviations. The cause of such bad pixels is typically lattice defects that create charge traps with high leakage current, or edge effects near the detector boundary. Since these small-pixel HCDs are engineering grade test devices with no screening, they are expected to have a fair percentage of bad and flickering pixels; the exact amount depends on the substrate voltage, as increased edge effects at higher substrate voltages lead to more such pixels. Between 2% and 4% of pixels were excluded during analysis of data from FPA 18568.

5. ANALYSIS AND RESULTS

5.1 Charge Spreading

As mentioned in Section 4, the small pixel size and large depletion depth of these detectors leads to a large amount of natural charge spreading. The charge cloud of an X-ray interacting in the silicon absorbing layer has both a large vertical distance to spread over, and a small horizontal distance before reaching nearby pixels, leading to a high percentage of multi-pixel events. This is typically non-ideal because it requires summing charge from multiple pixels to reconstruct an X-ray photon's energy, and therefore degrades energy resolution due to including noise from all pixels in the event.

The value of the substrate voltage (VSUB) can have a significant effect on the average number of pixels in an X-ray event. Higher VSUB will provide a stronger electric field that will cause the charge cloud to reach the ROIC sense node with less lateral diffusion into surrounding pixels. If one were aiming to have the best energy resolution and photon response at the softest X-ray energies, one would ideally raise VSUB to a level where the average final charge cloud size is completely contained in the size of a single pixel. However, it should be noted

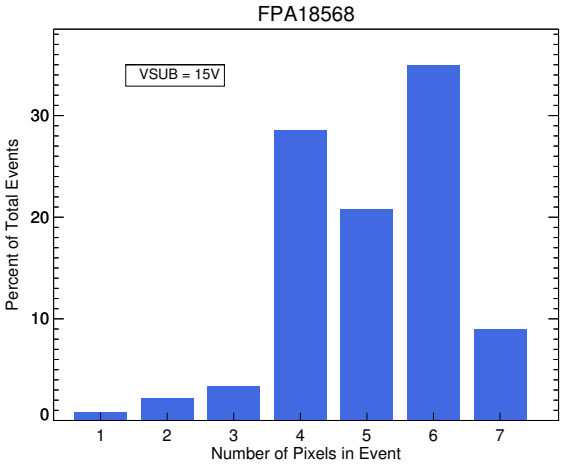

Figure 5. Charge spreading for FPA 18568 with VSUB = 15 V.

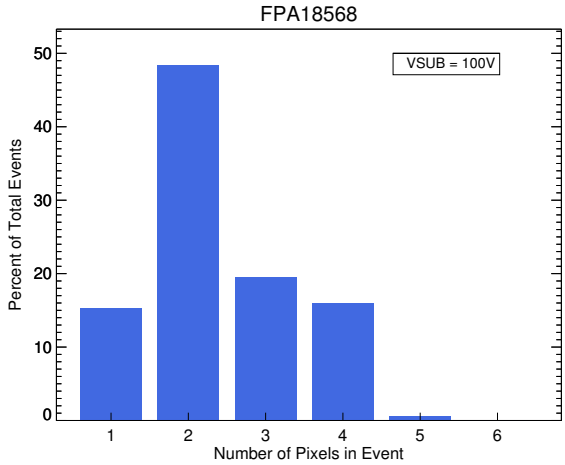

Figure 6. Charge spreading for FPA 18568 with VSUB = 100 V.

that better sub-pixel spatial resolution can be achieved through the use of multiple pixel events (Bray et al. 2018, these proceedings).[11]

We tested FPA 18568 at a range of VSUB values from 15V to 100V while collecting Mn Kα and Mn Kβ photons. X-ray events were graded to determine the number of pixels in each event. Events that spread to 4-6 pixels dominated images at VSUB = 15V (see Figure 5). However at VSUB = 100V, 5+ pixel events were virtually eliminated and there was a dramatic increase in 1 and 2 pixel events (see Figure 6). Results showing the percentage of events with 1-4 pixels as a function of VSUB are shown in Figure 7. It becomes practical to select only grade 0 and grade 1-4 events at VSUB $\approx$ 50V, while grade 0 events alone start to become significant at VSUB $\approx$ 70V. There may be even more to gain from yet higher VSUB values; current breadboard components limit VSUB to 100V, however future testing may push beyond this value.

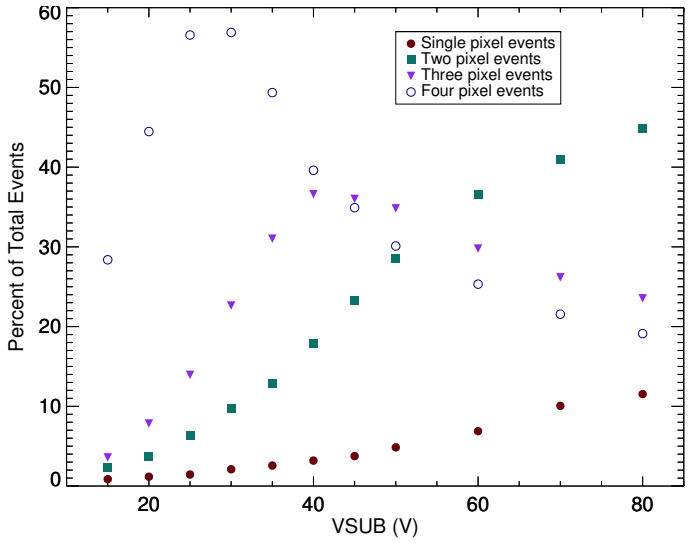

Figure 7. The percentage of total events that include 1 through 4 pixels as a function of VSUB for FPA 18568.

5.2 Energy Resolution

After event grading, energy spectra can be created for each pixel type and shielding level. The energy resolution is calculated by fitting Gaussian distributions to the Mn Kα and Kβ peaks. The energy resolution (ΔE) is then

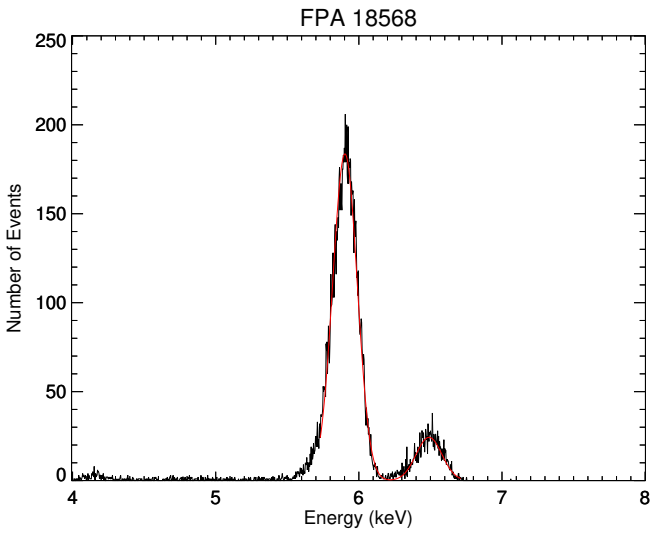

Figure 8. FPA 18568 energy spectrum with grade 0 events (VSUB = 100V) showing Mn Kα and Mn Kβ lines at 5.9 and 6.49 keV. The measured ΔE (FWHM) = 201 eV ± 4 eV with $\Delta E/E$ = 3.4% ± 0.1%. The two Gaussian fit is shown in red. Note that this energy spectrum is produced prior to gain variation correction (see Section 5.4).

defined as the full-width-half-maximum (FWHM) of the peak, given by $\Delta E = 2\sqrt{2\ln 2}\sigma$, where σ is the standard deviation of the Gaussian fit to the line at energy E.

The energy resolution at 5.9 keV for each pixel type and shielding level of FPA 18568 is summarized in Table 1. These data were taken with VSUB = 15V and processed with a 3σ secondary threshold that included all event grades that could be from real X-rays. Due to using all X-ray events in these spectra and therefore summing charge (and noise) from many pixels, energy resolution is somewhat degraded. We can see that type B (in-pixel CDS) pixels with additional shielding were the best performers, achieving 4.0% energy resolution at 5.9 keV. Type B pixels with less shielding had the worst performance, while both shielding level type A pixels performed similarly and at level in between the two type B pixels.

As seen in Section 5.1, selecting only grade 0 or grade 1-4 events is not practical at VSUB = 15V, yet is possible at higher VSUB values. Energy resolution was also measured at VSUB = 100V, where single pixel events account for 15% of total events and single plus two pixel events account for 64% of total events. Energy spectra consisting of only grade 0, and grade 0-4 events were created from these images (3σ secondary threshold), and then fit with Gaussians as described above. The energy resolution measurements are shown in Table 2. We find that for the preferred pixel type (type B with extra shielding), selecting only grade 0 events improves energy resolution to 3.4% (see Figure 8). If we select grade 0 and grade 1-4 events, the energy resolution is only slightly degraded, while a much larger fraction of the X-ray events are retained.

FPA 18568 (all X-ray events)

Pixel Type	Shielding	ΔE (eV)	$\Delta E/E$
A	Extra	278 ± 4	4.7% ± 0.1%
	Less	288 ± 4	4.9% ± 0.1%
B	Extra	237 ± 5	4.0% ± 0.1%
	Less	325 ± 7	5.5% ± 0.1%

Table 1. Measured energy resolution at 5.9 keV for FPA 18568 (VSUB = 15V), using all valid X-ray events. Note that these values are prior to gain variation corrections (see Section 5.4).

FPA 18568

Pixel Type	Shielding	Grades	% of Total Events	ΔE (eV)	$\Delta E/E$
B	Extra	0	15%	201 ± 4	3.4% ± 0.1%
		0 to 4	64%	207 ± 3	3.5% ± 0.1%

Table 2. Measured energy resolution at 5.9 keV for FPA 18568 (VSUB = 100V) with a 3σ secondary threshold. Only results for the preferred pixel type (type B with extra shielding) are shown.

5.3 Read Noise

Read noise is associated with the charge-to-voltage conversion step of X-ray detection. It can arise at various points along the readout chain from when charge enters the ROIC sense node to eventual conversion of voltage to a digital value. It effectively sets the noise floor of the detector and also directly impacts the energy resolution.

To measure the read noise, 1000 dark exposures that contained no X-ray events were collected for each pixel type and shielding level and then processed with the normal subtraction and boxcar smoothing algorithms. A cumulative dark frame histogram is then created and fit with a Gaussian to determine the standard deviation σ, which is a measurement of the read noise in units of Digital Number (DN). This method of measuring the read noise, in contrast to other methods such as the mean of the pixel-by-pixel RMS value, is insensitive to bad pixels and primarily samples the main pixel distribution.

The read noise was then converted to units of electrons using the standard conversion factor (3.65 eV/e^-)[12] and the measured Mn Kα peak centroid value. Table 3 summarizes the results. The read noise for all pixel types is fairly similar; measurements tend to be approximately 5.5 to 6.5 e^-, with the best measured value equal to 5.54 e^- ± 0.05 e^-.

FPA 18568

Pixel Type	Shielding	Read Noise (e^-)
A	Extra	5.57 ± 0.04
	Less	5.54 ± 0.05
B	Extra	5.85 ± 0.05
	Less	6.55 ± 0.09

Table 3. Measured read noise for FPA 18568 using a Gaussian fit to the cumulative dark frame noise histogram.

5.4 Gain Variation

HCDs make use of an individual readout amplifier in every pixel of the array, and although every amplifier in the array is designed to the same specifications, the amplifier gain will vary slightly across the detector. These differences in gain will lead to X-ray photons of the same energy being measured to have slightly different energies at different pixels. The net effect will be a degradation of the energy resolution, and if the gain variation is large enough this may even dominate over read noise in determining peak width. However, gain can be measured on a pixel-by-pixel basis and therefore corrections may be applied to account for the variation.

We used the HDL-5 test setup with an ^{55}Fe source to measure the gain variation of FPA 18568 type B pixels. Approximately 3000 Mn Kα grade 0 events per pixel were detected in over 250 hours of data. Because of the vast amount of data, event detection, grading, and histogramming were done in real time as images were captured, allowing images to be discarded without saving. In this way a Mn X-ray spectra was built up for each pixel in the array, allowing the Mn Kα and the noise peak to be fit with Gaussians. The gain was measured in each pixel by subtracting the centroid of the Kα peak from the centroid of the noise peak, and then dividing by the estimate of 1616 e^- per event (assuming $\omega = 3.65$ eV/e^- with $E = 5.9$ keV).

A gain variation map was created for FPA 18568 and then the gain variation was calculated as the standard deviation of the gain variation map divided by the mean gain (excluding inactive pixels). Gain variation was found to be 1.23% ± 0.10% for all active pixels, 1.12% ± 0.06% for just extra shielding pixels, and 1.19% ± 0.05% for just less shielding pixels. Figure 9 shows the calculated gain variation map for FPA 18568, while Figure 10 shows the pixel gain histogram.

Figure 9. Gain variation map for FPA 18568. Brightness of pixels corresponds to the gain measured in a pixel. The measured gain variation (excluding inactive pixels — many seen at array edges) is 1.23% ± 0.1%.

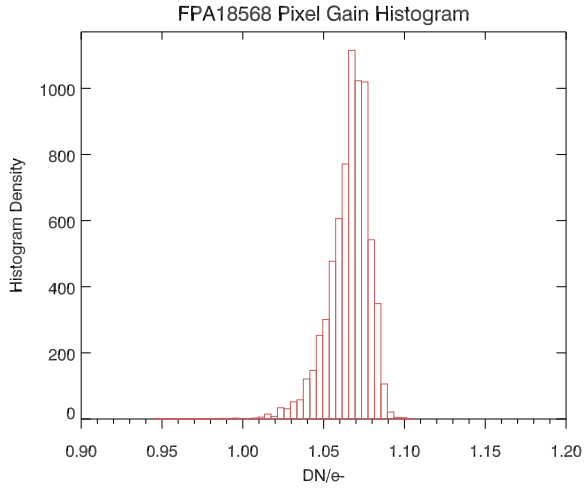

Figure 10. Gain histogram for FPA 18568 type B pixels. The gain variation was found to be 1.23% ± 0.10% for all active pixels. Pixels with only extra shielding have 1.12% ± 0.06% gain variation, while pixels with only less shielding have 1.19% ± 0.05%. gain variation.

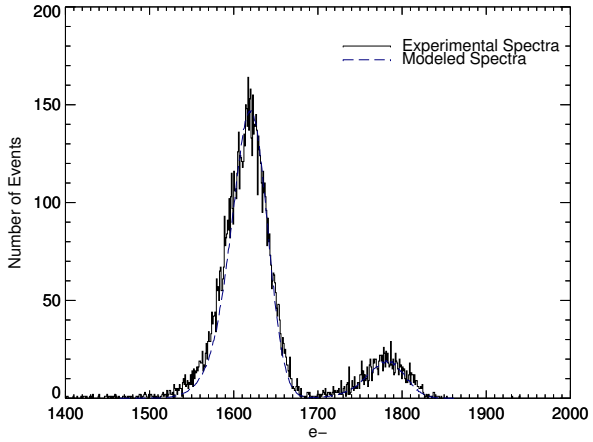

Figure 11. Experimental (black solid line) and Monte Carlo modeled spectra (blue dashed line) for FPA 18568 type B pixels with extra shielding (grade 0 events). The experimental spectrum has $\Delta E/E = 3.4\%$, while the modeled spectrum has $\Delta E/E = 3.1\%$.

5.4.1 Gain Variation Modeling

It is possible to model the effect of gain variation on the energy resolution. Assuming negligible dark current, the energy resolution of the detector is given by

$$\frac{\Delta E}{E} = \frac{2.354\omega}{E}\sqrt{\frac{FE}{\omega} + \sigma^2 + \left(\frac{GV \times E}{\omega}\right)^2} \tag{1}$$

where $\omega = 3.65$ eV/e$^-$, F is the Fano factor (0.115 for silicon[13]), E is the incident photon energy, σ is the read noise, and GV is the gain variation. For a 5.9 keV X-ray, and assuming the values for type B extra shielding pixels ($\sigma = 5.85$ e$^-$ and $GV = 0.0112$), the predicted energy resolution is 3.37%, in excellent agreement with the measured grade 0 events energy resolution in Section 5.2.

Monte Carlo simulations can also be used to model the effect of gain variation. A pixel gain distribution was created matching the slightly non-Gaussian distribution from gain variation map in Figure 10. In addition, an X-ray event distribution was created consisting of two Gaussians with means at 1616 e^- and 1778 e^- (the Mn Kα and Mn Kβ centroids), and standard deviations equal to the combination, in quadrature, of the Fano noise term and the measured read noise. The X-ray event distribution was convolved through the pixel gain distribution to create a modeled energy spectrum. This modeled spectrum is seen in Figure 11 compared to the experimentally obtained spectrum, which it reproduces fairly well — including most of the low energy tail. The slightly higher tail in the experimentally obtained spectrum most likely arises from events that lost a small amount of charge to neighboring pixels. The modeled spectrum was fit with the standard two Gaussian fit, finding ΔE (FWHM) = 3.1% at 5.9 keV, in fairly close agreement with the experimentally measured value.

5.4.2 Gain Variation Correction

With the gain variation map in hand, it is also possible to create energy spectra that have been corrected for the effects of gain variation. The data reduction procedure is modified slightly; prior to boxcar smoothing subtracted images, each image is multiplied by a gain map that converts the image to electron space, after which boxcar smoothing continues and the same steps outlined in Section 4 take place. Figure 12 show the results of this correction applied to FPA 18568 type B pixels with extra shielding, selecting only grade 0 events and using a 3σ secondary threshold. We achieve energy resolution of 158 eV (2.7%) at 5.9 keV using this correction.

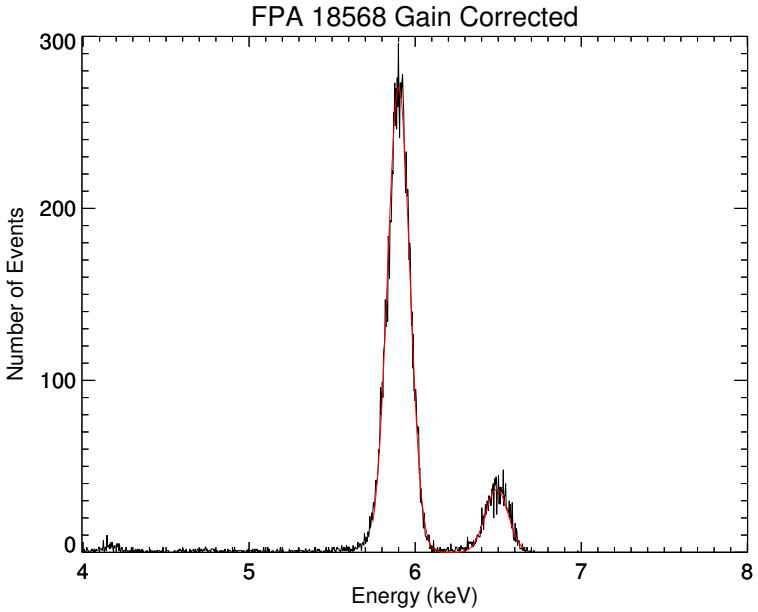

Figure 12. FPA 18568 energy spectrum with only grade 0 events (VSUB = 100V) that has been corrected for pixel-to-pixel gain variation. The Mn Kα and Mn Kβ lines at 5.9 and 6.49 keV are fit with two Gaussians, shown in red. The measured ΔE (FWHM) = 158 eV ± 4 eV with $\Delta E/E$ = 2.7% ± 0.1%.

FPA 18568 Gain Corrected

Pixel Type	Shielding	Grades	Secondary Threshold	% of Total Events	ΔE (eV)	$\Delta E/E$
B	Extra	0	2σ	11%	148 ± 6	2.5% ± 0.1%
			3σ	15%	158 ± 4	2.7% ± 0.1%
		0 to 4	2σ	51%	157 ± 5	2.7% ± 0.1%
			3σ	64%	165 ± 3	2.8% ± 0.1%

Table 4. Measured energy resolution at 5.9 keV for FPA 18568 (VSUB = 100V), after applying gain variation correction.

If the gain variation had been perfectly corrected for, we would expect to be able to predict the resulting resolution using equation 1 with $GV = 0$. This results in a theoretical $\Delta E/E = 2.1\%$, which is not achieved by our correction. There is error associated with measuring the gain map that will factor into this difference, in addition to our measured spectra likely having some events that lost a small amount of charge to neighboring pixels that were not summed into the event, leading to slight peak broadening. Lowering the secondary threshold can help to lessen this effect at the cost of cutting out more events. Lowering the secondary threshold from 3σ to 2σ, we achieve 148 eV (2.5%) resolution at 5.9 keV — the best energy resolution at 5.9 keV measured to date for an X-ray HCD — at the cost of going from using 15% of total events to using 11% of total events. Table 4 summarizes the results of the gain variation correction.

6. CONCLUSIONS

We have reported results for one of the new prototype small pixel hybrid CMOS X-ray detectors. All four pixels types were successfully operated, which allowed for determination that pixels with in-pixel CDS and extra shielding performed the best. The amount of charge spreading has been characterized as a function of applied substrate voltage. We find that increasing substrate voltage to $\gtrsim$ 50V allows for grade 0 to 4 events to form a significant fraction of total events. We also measure read noise to be as low as 5.54 e^- and have characterized the the pixel-to-pixel gain variation to be $\sim$ 1.1%. Gain variation corrected spectra were measured to have energy resolution as good as 148 eV (2.5%) at 5.9 keV — making both the energy resolution and read noise measurements reported here the best yet obtained for an X-ray HCD.

These results are promising for the application of X-ray hybrid CMOS detector technology for *Lynx* and other future X-ray missions. X-ray HCDs already meet the fast readout needs of large effective area missions, and these prototypes have demonstrated that high performance can be maintained with small enough pixel sizes to properly sample fine resolution X-ray mirrors. Moreover, the read noise and energy resolution requirements of HDXI on *Lynx* are only slightly more exacting than the performance currently achieved here. Work to further reduce X-ray HCD read noise is an active area of development for future generation X-ray HCDs.

ACKNOWLEDGMENTS

We gratefully acknowledge support from that NASA APRA Detector Development Program, particularly support from grant numbers NNX13AE57G and NNX16AE27G. We would also like to acknowledge Vincent Douence and Mihail Milkov for contributions to the operation and design of the small pixel HCDs.

REFERENCES

[1] Gaskin, J. A., Dominguez, A. D., Gelmis, K., Mulqueen, J., Swartz, D. A., McCarley, K. S., Ozel, F., Vikhlinin, A., Schwartz, D. A., Tananbaum, H. D., Blackwood, G. H., Arenberg, J. W., Purcell, W., and Allen, L., "The Lynx X-ray Observatory: concept study overview and status," *Proc. SPIE* **10699**(21) (2018).

[2] Loose, M., Farris, M. C., Garnett, J. D., Hall, D. N. B., and Kozlowski, L. J., "HAWAII-2RG: a 2k x 2k CMOS multiplexer for low- and high-background astronomy applications," *Proc. SPIE* **4850**, 13 (2003).

[3] Kozlowski, L. J., Loose, M., Joshi, A. B., Vural, K., and Buchin, M. P., "Low-power system-on-a-chip FPAs," *Proc. SPIE* **4820**, 10 (2003).

[4] Bai, Y., Bajaj, J., Beletic, J. W., Farris, M. C., Joshi, A., Lauxtermann, S., Petersen, A., and Williams, G., "Teledyne imaging sensors: silicon CMOS imaging technologies for x-ray, UV, visible, and near infrared," *Proc. SPIE* **7021**, 16 (2008).

[5] Prieskorn, Z. R., Bongiorno, S. D., Burrows, D. N., Falcone, A. D., Griffith, C. V., and Nikoleyczik, J., "Soft x-ray quantum efficiency of silicon hybrid CMOS detectors," *Proc. SPIE* **9154**, 7 (2014).

[6] Griffith, C. V., Falcone, A. D., Prieskorn, Z. R., and Burrows, D. N., "The Speedster-EXD- A New Event-Driven Hybrid CMOS X-ray Detector," *Journal of Astronomical Telescopes, Instruments, and Systems* **2**(1), 016001 (2016).

[7] Falcone, A. D., Burrows, D. N., Bai, Y., Farris, M., Cook, R., and Bongiorno, S., "Hybrid CMOS x-ray detectors: the next generation for focused x-ray telescopes," *Proc. SPIE* **6686**, 6 (2007).

[8] Prieskorn, Z. R., Griffith, C. V., Bongiorno, S. D., Falcone, A. D., and Burrows, D. N., "Characterization of Si hybrid CMOS detectors for use in the soft x-ray band," *Nuclear Instruments and Methods in Physics Research A* **717**, 83–93 (2013).

[9] Griffith, C. V., Falcone, A. D., Prieskorn, Z. R., and Burrows, D. N., "Recent progress and development of a speedster-EXD: a new event-triggered hybrid CMOS x-ray detector," *Proc. SPIE* **9601**, 9 (2015).

[10] Burrows, D. N., Hill, J. E., Nousek, J. A., Kennea, J. A., Wells, A., Osborne, J. P., Abbey, A. F., Beardmore, A., Mukerjee, K., Short, A. D. T., Chincarini, G., Campana, S., Citterio, O., Moretti, A., Pagani, C., Tagliaferri, G., Giommi, P., Capalbi, M., Tamburelli, F., Angelini, L., Cusumano, G., Bräuninger, H. W., Burkert, W., and Hartner, G. D., "The Swift X-Ray Telescope," *Space Science Reviews* **120**(3), 165–195 (2005).

[11] Bray, E., Falcone, A. D., Hull, S. V., and Burrows, D. N., "Exploring Fine Subpixel Spatial Resolution of Hybrid CMOS Detectors," *Proc. SPIE* **10699**(204) (2018).

[12] Janesick, J., [*Scientific Charge-Coupled Devices*], SPIE Press, Bellingham, Washington (2001).

[13] Fraser, G., Abbey, A., Holland, A., McCarthy, K., Owens, A., and Wells, A., "The x-ray energy response of silicon part a. theory," *Nuclear Instruments and Methods in Physics Research Section A: Accelerators, Spectrometers, Detectors and Associated Equipment* **350**(1), 368 – 378 (1994).